Silicon (2022) 14:9925–9941
https://doi.org/10.1007/s12633-022-01717-4

ORIGINAL PAPER

Effect of Multipass FSP on Si-rich TIG Welded Joint of Dissimilar Aluminum Alloys AA8011-H14 and AA5083-H321: EBSD and Microstructural Evolutions

Abdellah Nait Salah[1] · Sipokazi Mabuwa[2] · Husain Mehdi[3] · Velaphi Msomi[2] · Mohammed Kaddami[1] · Prabhujit Mohapatra[4]

Received: 2 January 2022 / Accepted: 24 January 2022 / Published online: 12 February 2022

Abstract
In this analysis, friction stir processing (FSP) was applied to the Si rich TIG welded joint to study the influence of multi-pass FSP (MPFSP) on microstructure, hardness and tensile properties. The TIG welding defects (coarse grain structure, porosity, microvoids, and solidification cracking) were eliminated, and the grain size of the TIG welded joint was decreased. As the FSP passes increases, the coarse eutectic Mg_2Si and $Al_{13}Fe_4$ phases are converted into small phases. The coarse and elongated dendrite structure of the TIG welded joint was decreased after one FSP pass. The homogenization or modification of the primary α-Al exists in the TIG weldment was continuously improved as the TIG + FSP pass increased. The SZ of TIG + 3 pass FSP showed ultrafine grains of 3.42 µm compared to other welded specimens. The average ultimate tensile strength (UTS) of the TIG welded joint with filler ER4043 was observed to be 79.82 MPa, whereas the UTS of TIG + 1 pass FSP, TIG + 2 pass FSP, and TIG + 3 pass FSP was 97.87 MPa, 120.36 MPa, and 126.92 MPa respectively.

Keywords Friction stir processing · Tensile strength · Microstructure · Microhardness

1 Introduction

Aluminum alloys are versatile materials used in structural components, automotive parts, maritime components, and aerospace parts [1–3] because they have better formability, high toughness, good corrosion resistance and high specific strength. Furthermore, the mechanical properties of aluminum alloys can be improved by natural or artificial aging and solution treatment. There are various aluminum alloys available on the market depending upon alloying elements. These aluminum alloys possess different mechanical, electrical, and chemical properties with diverse industrial applications. Recently, AA5083, containing Al–Mg, and AA8011 containing Al–Fe, has emerged as the basic structural aluminum alloy in modern engineering applications. AA5083 is used in pressure vessels, drilling rigs, shipbuilding, railroad cars, etc., whereas AA8011 is used in transportation and construction work [4, 5]. Various nanoparticles were employed during friction stir processing to enhance the mechanical properties, microstructure, and wear behavior of the base metal [6–8]. The Al–Mg and Al–Fe-based alloys AA5083-H321 and AA8011-H14 have excellent corrosion resistance, moderate strength, and high ductility [9]. The fusion welding of aluminum alloys presents a prodigious challenge for investigators. Tungsten inert gas (TIG) welding is an appropriate technique for aluminum alloy welding, and it has wide application in various industries [10]. The defects observed in TIG welded joints are high residual stress, solidification shrinkage, coarse grain structure, aluminum oxide, and micro-cracks [11]. Various conventional/unconventional welding processes, i.e., laser-TIG hybrid welding [12, 13], laser beam welding [14], TIG welding [15], friction stir welding (FSW) [16], TIG + FSP welding [17–20],

✉ Husain Mehdi
husainmehdi4u@gmail.com

1 Faculty of Science and Technology, Laboratory "Physical Chemistry of Processes and Materials", Hassan First University of Settat, Settat, Morocco

2 Mechanical Engineering Department, Cape Peninsula University of Technology, P.O. Box 1906, Bellville 7535, South Africa

3 Department of Mechanical Engineering, Delhi Technological University, Delhi, India

4 School of Advanced Sciences, VIT University, Vellore, India

Table 1 Chemical composition of AA5083 and AA8011

BM	Si	Fe	Cu	Mn	Mg	Cr	Ti	Zn	Al
AA5083	0.139	0.153	0.010	0.649	4.339	0.040	0.011	0.013	Bal
AA8011	0.421	1.119	0.106	0.549	0.326	0.027	0.015	0.079	Bal
ER4043	5.2	0.74	0.25	0.04	0.04	0.01	0.15	0.1	Bal

have been applied to join aluminum alloys. Among these processes, the TIG welding process is commonly employed for aluminum alloys in terms of economy and utility. In TIG welding process, penetration occurs in the weldment and it may increase as the heat input increases. Due to high heat input, the coarse grains, formation of porosity, and wide heat affected zone were observed, which depreciate the UTS of the weldment. Numerous works have been published to improve the UTS and grains structure of the TIG welded aluminum alloy joints, i.e., using welding flux to rise the penetration [21], taking double side TIG welding to remove porosities, optimizing the welding process parameters [22, 23], post or preheat treatment to enhance the grain structure of the welded region [24, 25]. Conversely, in many cases, the joint efficiency of the weldment was found to be lesser than the parent material due to the unlike grain structure between the welded joints and the parent metals. The brittle interdendritic structure was observed due to re-solidification and eutectic melting of the fusion zone (FZ), which affects the hardness, ductility, and UTS [26, 27]. To remove these defects, FSW/FSP was introduced in 1991 at the Welding Institute in the U.K. by Wayne Thomas [28]. Friction stir processing (FSP) makes the material undergo severe plastic deformation, leading to a homogenous refined microstructure via stirring and frictional heat during processing [29]. During this process, a rotating tool comprising of a tool pin enters into the base plate and moves in the welding direction with constant tool rotational speed. The base metal in front of the tool pin transmits backward because linear motion and tool pin rotation are subjected to forging and extrusion under a high strain rate. Hence, the FSPed zone exhibited increased tensile properties and fatigue life of the processed region due to the enhancement of microstructure [30, 31]. There is no melting point of metal during FSP, which effectively avoids defects such as thermal cracks and porosities that are generated during the melting and solidification of the metal. FSP is a microstructure modification technique that eliminates the defects in the existing base plate and enhances the tensile properties and hardness value of the base metal. Low welding speeds with high tool rotational speeds (TRS) were used to fabricate the dissimilar aluminum alloys AA2219 and AA5083 and observed defect-free joints with 97% joint efficiency [32]. The non-heat-treatable alloy AA5083 has the highest strength, but it is not recommended for use in temperatures above 70° C. This alloy retains exceptional strength after welding compared to other aluminum alloys

Table 2 Mechanical properties of the alloys

BM	UTS (MPa)	Strain (%)	Hardness (HV)
AA5083	320.891	27.9	91.373
AA8011	93.07	39.1	31.820

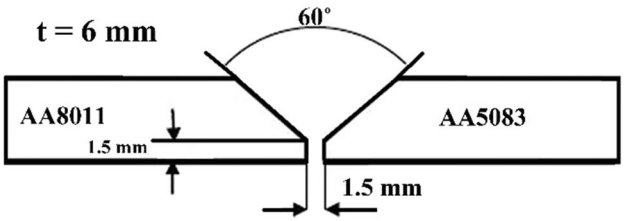

Fig. 1 Design and dimension of V groove

[33]. The tensile properties and grain structure of the dissimilar welded joints of AA8011/AA6082 were enhanced by submerging friction stir processing and results revealed that the grain size decreased compared to base metal and FSWed joints [34]. Most of the research scholars have analyzed that all these techniques enhance the material strength but decrease their ductility because large defect volumes develop after deformation, resulting in premature plastic instability and little strain hardening [35–38]. Very limited work has been done on the FSWed joints of AA5083 and AA8011. During this study, the focus was made on the effect of FSP on the tensile properties, microhardness and grain structure of the TIG welded joints.

2 Materials and Method

The aluminum alloy grades used were AA5083-H321 and AA8011-H14, with a plate thickness of 6 mm. The chemical composition and mechanical properties of the base materials were predetermined prior to the study, refer to Tables 1 and 2 respectively. The said materials were cut into dimensions of 250 × 52 mm to accommodate the bed of the FSP fixture/jig. The dissimilar cuts of the plates were prepared into a single v-groove as depicted in Fig. 1. The JavWeld pulsed TIG welding machine was used to fabricate the TIG welds. The parameters used for the TIG and TIG + FSP welding process are shown in Table 3. Three TIG- welded plates were produced, one to be kept as is and the other two to

Table 3 TIG and TIG + FSP welding parameters

Parameter	
Filler wire	AA4043
Wire diameter (mm)	2.5
Shielding gas	Argon
Welding current (Amps)	120
Gas flowrate (L/min)	25
Welding speed (mm/min)	40
Voltage (V)	35
Tool rotational speed (rpm)	1450
Too traverse speed (mm-min^{-1})	105

be used later for FSP. The fabricated TIG-welded plate is presented in Fig. 2b.

Figure 2c shows the milling machine, LAGUN FU.1-LA model, that was used for FSP. The square FSP tool was used for the processing of the TIG welds. Figure 3 show the FSP tool profile. The dimensions of the tool included a tool shoulder diameter of 20 mm, a tool pin length of 5.6 mm, and a 7 mm tool pin diameter. It should be noted that two different material positioning were taken into consideration during the FSP of the TIG welds. Figure 2e shows TIG + FSP welds. The produced TIG and TIG + FSP plates were cut for different tests, including XRD, microstructure electron backscatter diffraction (EBSD), microhardness, and tensile tests. Prior XRD chemical composition of the produced weld was analyzed using the Belec compact port. The Motic AE2000 metallurgical light optical microscope was used for microstructural examination. The grain orientation, grain size, and grain boundary structure were examined by the EBSD process. The samples for EBSD analysis were electro polished at 15 V for 35–40 s at 25 °C in a mixed solution of 30% HNO_3 + 70% CH_3OH, and then examined. The microstructure grain sizes were measured using the Image J software, adapting the line intercept method as described in the ASTME112-12 standard. Prior to the examination, the specimens were metallurgical prepared and etched using sodium hydroxide and modified Keller agents. The composition of the NaOH included the 2 g of NaOH and 100 ml of distilled water, while the modified Kellers consisted of 10 ml of HNO_3, 1.5 ml HCl, 1 ml of HF, and 87.5 ml of H_2O. The microhardness was measured using the Innova Test Falcon 500 Vickers hardness testing machine, and the ASTME384-11 standard. A mass of 0.3 kg, a 1 mm spacing between points, and a single line was used. A total of 20 indentations were measured from base metal to weld ceneter. The

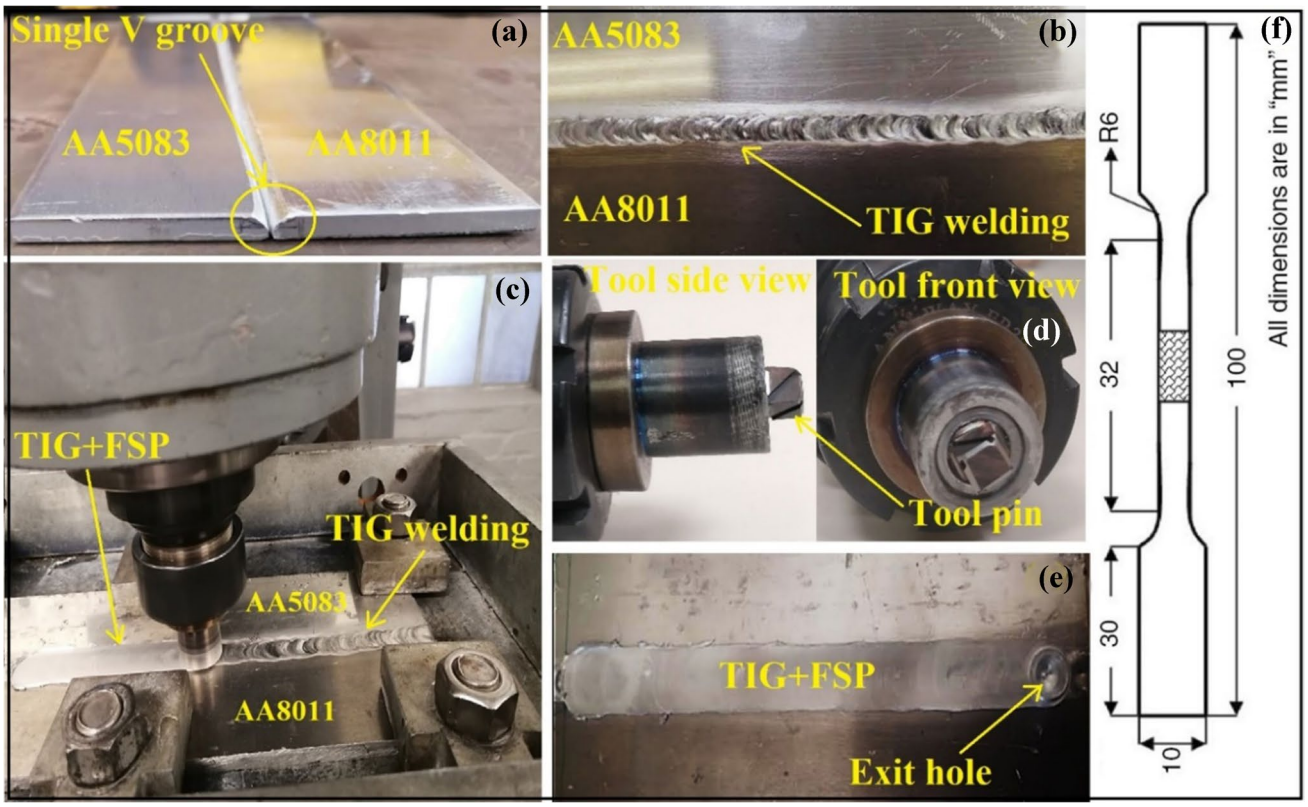

Fig. 2 Experimental process of TIG and TIG + FSP welded joints, (**a**) V groove of 60° for TIG welding, (**b**) TIG weldment with filler ER4043, (**c**) TIG + FSP process, (**d**) tool used during FSP, (**e**) TIG + FSP welded joint, (**f**) tensile sub test specimen

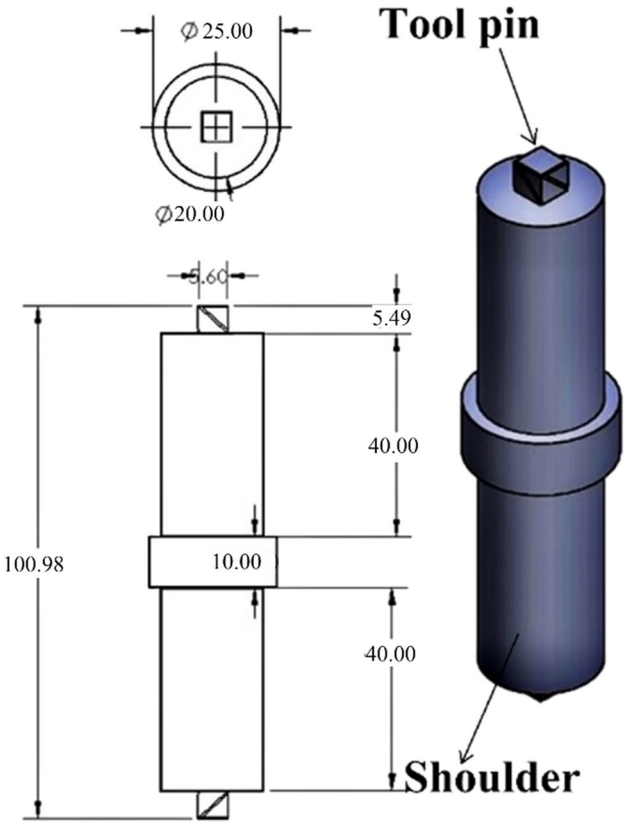

Fig. 3 Design and dimension of FSP tool

Hounsfield 50 K machine was used for tensile testing. The tensile testing was conducted with reference to the ASTM E8M-04 standard as shown in 1f.

3 Microstructural observation

3.1 Microstructural characterization of TIG and TIG + FSP welded joints

The optical images of the cross-section of the TIG weldment of AA5083 and AA8011 is shown in Fig. 4, and it was noticed that welding parameters, controlling the intermetallic distribution, and heat input have a prominent role in the broadening of grain size and partially melted zone (PMZ) [39, 40]. As the heat input increases, the size of the PMZ flares away, and the grain structure coarsens [41]. This results in poor UTS and a decrease in sample hardness in the weld fusion zone. Image J software was used to examine the grain structure of the different welded zones. The microstructure of the base metal (AA8011 and AA5083) was obtained by optical and SEM observation. The average grain size of the AA8011 and AA5083 exhibits 114 µm and 98 µm respectively (Table 4).

The microstructure of different zones of TIG-welded joints of AA5083 and AA8011 is revealed in Fig. 4, which exhibits the microstructures of the fusion zone and weld zone. The fusion zone is a semi-molten region between the HAZ and WZ that preserves severe inhomogeneity physical and chemical properties, which reveals the transition tissue i.e., discontinuous banded structure. The microstructure of HAZ was illustrated in Fig. 4c, which revealed elongated and coarse grains formed by rolling. The grains dissemination in the HAZ is non-uniform and the grains were elongated and coarsened compared to the fusion zone. Most strengthening phases in the HAZ might be reduced by re-dissolution because of the rapid cooling and high temperature during the TIG welding.

The optical macrostructure of TIG + FSP with different zones SZ, and TMAZ is illustrated in Fig. 5. The sharp interface was observed between the TMAZ and SZ on the advancing side (AS) and uncertain on the retreating side (RS), which demonstrates that the advancing side has some larger gradients of temperature and strain [42, 43]. The slop of the interface between the TMAZ and SZ was larger on the RS, which may be attributed to the different material flows on both sides [44]. The TMAZ region experienced weaker deformation, and heating effects than the SZ, and partial recrystallization and dynamic recovery took place at TMAZ. Hence, elongated deformation and equiaxed DRX grains were observed in the TMAZ region. The grain size of the TIG + 1FSP, TIG + 2FSP, and TIG + 3FSP joints at the SZ exhibits 10.85 µm, 6.95 µm, and 3.42 µm respectively, which reveals that the microstructure in the SZ may have refined for increased strain by applying the FSP. During FSP, the coarse eutectic Mg_2Si precipitates dissolved completely into the AMC, forming a stronger diverse structure than the TIG weldment of AA5083 and AA8011. Friction stir processing is comprising heat generation and intense material flow obtaining from plastic deformation and frictional heat generated between the base plate and FSP tool [45]. The SZ reveals the basin-like bottom region shown in the dotted line. The microstructure of the TIG + FSP joints exhibits a defect-free region and observed homogenous and fine grain structure in the SZ, as shown in Fig. 6b-d.

Figure 7a reveals the high magnification SEM image of the TIG-weldment at the fusion zone and observed Mg_2Si precipitates at the grain boundaries. This intermetallic compound is commonly generated in aluminum alloys. Due to grain growth caused by input heat, the average grain size of the FZ and HAZ was 19.52 µm and 24.85 µm, respectively, which was less than that of the parent metals AA5083 and AA8011. The fusion zone's microstructure was characterized by globular primary α-Al and precipitated Mg_2Si, where α particles were found along the grain boundaries. The HAZ observed a larger thermal cycle than the fusion zone experiencing lesser α-Al particles in the HAZ and few

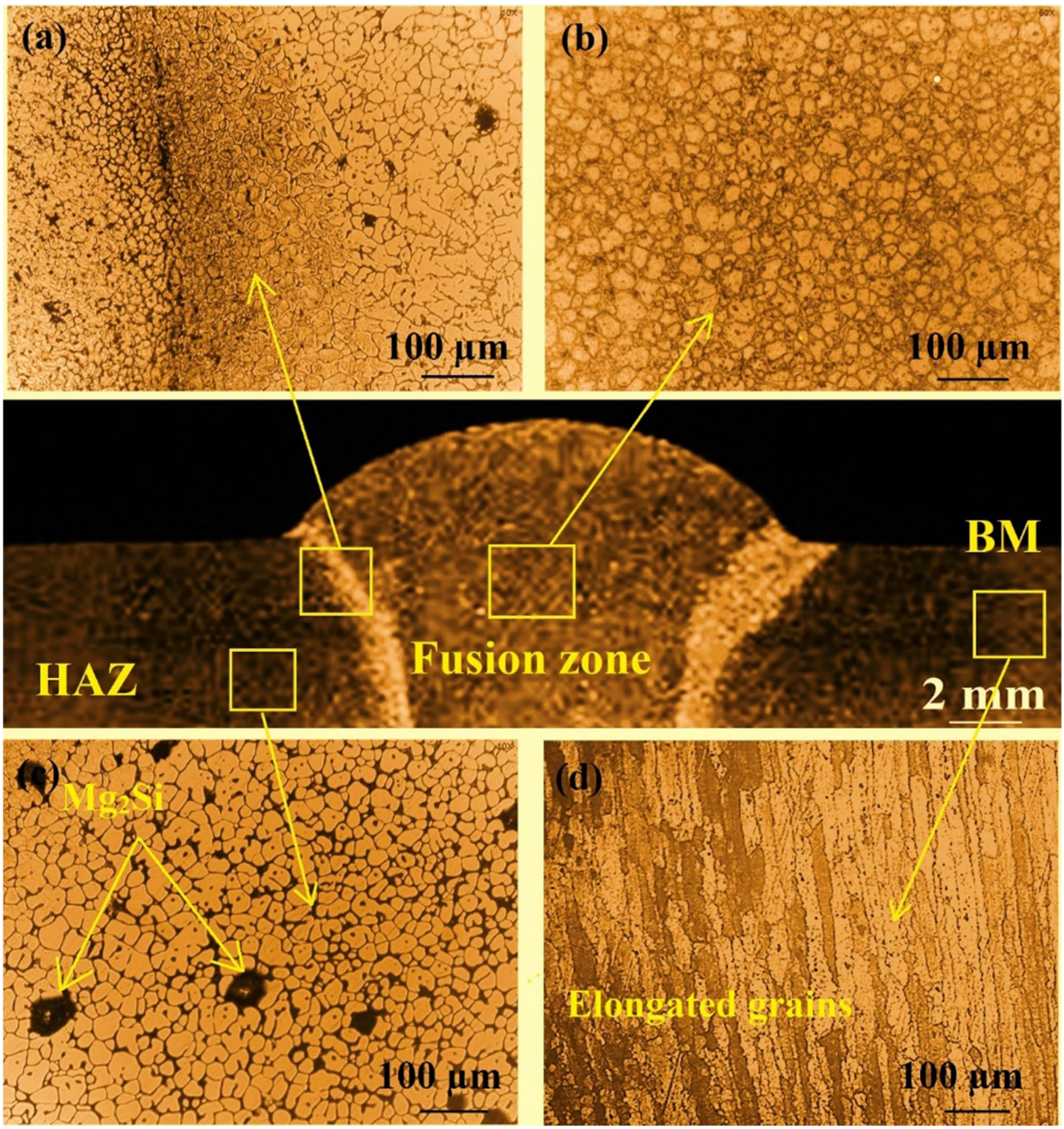

Fig. 4 TIG welded joint of AA5083 and AA8011 with filler ER4043, (**a**) different zone of TIG welding, (**b**) HAZ region, (**c**) fusion zone, (**d**) welding zone

α-particles precipitated out at grain boundary. The HAZ and fusion zone reveal different microstructures compared to base metals. Moreover, microspores of different diameters were generated in the fusion zone. The back surface was unable to be preserved by the shielding gas, whereas the top surface of the melting pool was preserved in the TIG welding process. Therefore, the air quickly entered the melting pool through the gap between the two plates. Due to the comparatively low cooling rate of the TIG welding process, hydrogen cannot have separated from the melting pool, which creates pores in the fusion zone, resulting in the formation of microfractures around the pores [46, 47].

The homogenization or modification of the primary α-Al exists in the TIG weldment of AA8011 and AA5083 was

Table 4 Mechanical properties of the TIG and TIG + FSP welded joints of AA5083 and AA8011

Materials	UTS (MPa)	Joint efficiency (%)	Strain (%)	Hardness (HV)	Grain size (μm)	Fractured location
AA5083	320.89	-	27.92	91 ± 2	98	-
AA8011	93.07	-	39.1	31 ± 3	114	-
TIG	79.82	85.76	24.95	52 ± 4	19.52	HAZ
TIG + 1 FSP pass	97.87	105.15	21.89	60 ± 2	10.85	TMAZ
TIG + 2 FSP pass	120.36	129.32	26.52	64 ± 4	6.95	Base material (AA8011)
TIG + 3 FSP pass	126.92	136.37	29.41	68 ± 3	3.42	Base material (AA8011)

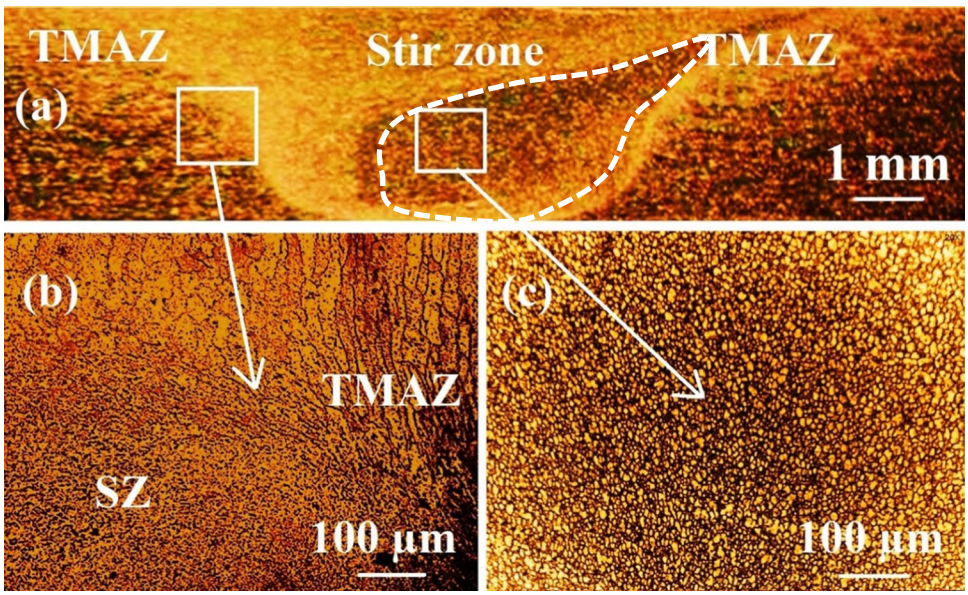

Fig. 5 Different zone of TIG + FSP welded joint

continuously improved as the TIG + FSP pass increased. The coarse and elongated dendrite structure of the TIG welded joint was decreased after one FSP pass, as shown in Fig. 7b. Due to the enhancement of material mixing and dispersion, the eutectic Mg_2Si precipitates were further decimated. The area fraction of the fine and equiaxed grains increases as the TIG + FSP pass increases, demonstrating a direct correlation between particle dispersion and FSP passes due to the reduction of eutectic Mg_2Si precipitates [48]. After the 3rd FSP pass, the coarse and elongated grain structure was completely converted into the fine and equiaxed microstructure illustrated in Fig. 7d. During multipass FSP, an incessant kind of strain was observed, leading to the breakdown of coarse and elongated grains, drastically reducing the grain size of the TIG + FSP welded joints of AA5083 and AA8011. Moreover, the MPFSP boosted the DRX mechanism and found fine grain structures [49]. A eutectic Mg_2Si precipitates with less formability than the parent material and is concerted within the grain boundaries observed in TIG welded joints (see Fig. 7a). The material flow was tough, and most precipitates remained at grain boundaries. They move near the SZ as an increment of FSP passes on the TIG weldment, observing more uniform dissemination and fewer clusters of eutectic Mg_2Si precipitates (Fig. 7b-d).

3.2 EDX analysis of TIG and TIG + FSP welded joints

Figure 8 reveals the energy-dispersive x-ray spectroscopy (EDX) of TIG-weldment of AA5083 and AA8011, and TIG + 3 pass FSP, where the atomic percentages of aluminum and silicon in the SZ and fusion zone were higher than the other elements. In TIG weldment, the percentage of Al is highest (91.82), Si is second highest (4.25%), and Mg is the third highest (3.12%). The alloying elements were uniformly diffused in TIG + 3pass FSP at the SZ. The alloying elements Mg, and Si generates the precipitates, and this precipitation intensity disseminated after one pass FSP, which enhanced the mechanical properties of the processed zone [50], the XRD study is shown in Fig. 11 verified this finding. The EDX was used in map scanning mode on the marked area of TIG and TIG + FSP weldment illustrated in Figs. 9 and 10 to analyze the distribution of the elements between

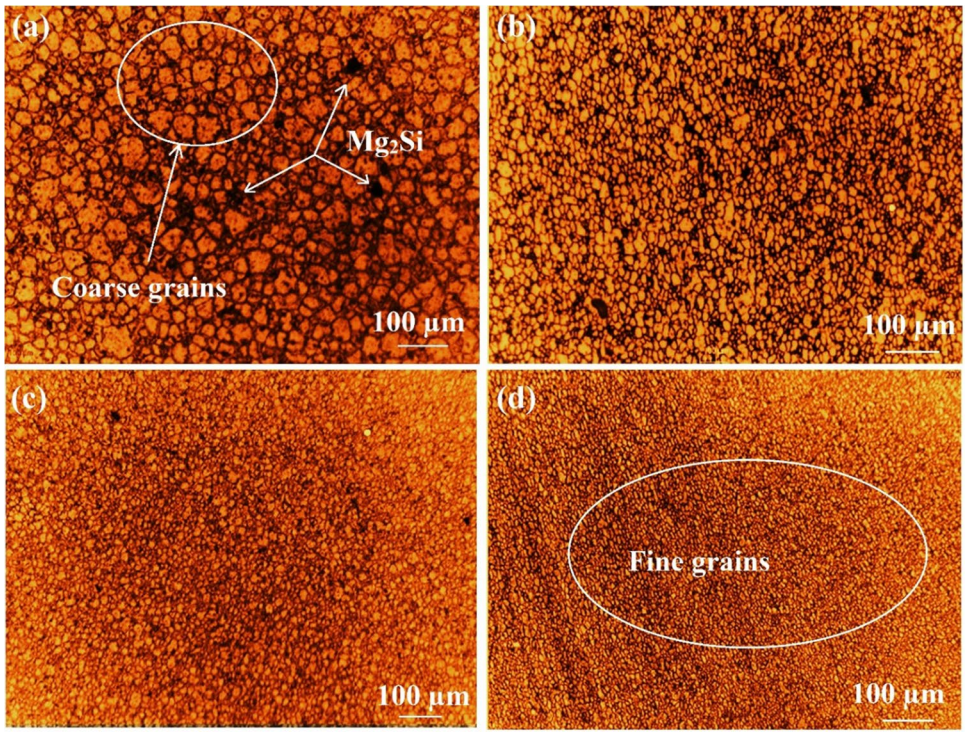

Fig. 6 TIG + FSP welded joint of AA5083 and AA8011, **a** HAZ of TIG + 1 FSP, **b** SZ of TIG + 1FSP, **c** SZ of TIG + 2FSP, **d** SZ of TIG + 3FSP

the different locations. In the fusion zone and the SZ, the primary elements are distributed. The aluminum content on the grain boundaries is lower than that within the grains. Figure 10 reveals that major alloying elements were more evenly disseminated in the SZ after the 3rd pass FSP compared to the TIG weldment.

3.3 XRD analysis

XRD (BRUKER D8 ADVANCE) was employed to phase identify the TIG and TIG + FSP welded joints Cukα radiation at 1.518 Å, illustrated in Fig. 11. Due to the unique d-spacing for each material, the conversion of the diffraction peaks to d spacing allows for the identification of the metal. The XRD peak of Mg_2Si revealed the disparately visible that confirmed the successful fabrication of TIG, and TIG + FSP welded joint with filler ER4043. The considerable presence of peaks corresponding to any other compound (except Al, Si, Mg_2Si, and $Al_{13}Fe_4$) was not observed in the XRD diagram, which showed the thermodynamic stability of Mg2Si, $Al_{13}Fe_4$. The phase identification of the TIG and TIG + FSP welded joints of AA5083 and AA8011 is illustrated in Fig. 11. Four major phases (Al, Si, Mg_2Si, and $Al_{13}Fe_4$) were detected in welded joints. The intensity of Mg_2Si, $Al_{13}Fe_4$ was reduced as the FSP pass increased from 1 to 3 passes. The penetration depth of TIG and TIG + FSP welded joints were evaluated by $\tau = \cos\psi 2\ \mu.\ \mathrm{Sin}\theta$ [51], where θ is the Bragg peak, μ is the coefficient of linear absorption, ψ is the tilt angle, and τ is the depth of mean penetration. The hardness values of the TIG + FSPed zone was influenced by strain hardening, precipitate formation, and boundary energy [52]. Figure 11 reveals no unfavorable reaction ensues between the dissimilar aluminum alloys AA5083 and AA8011. The phase intensity decreases as the FSP pass increases [53]. As the FSP passes increases, the coarse eutectic Mg_2Si and $Al_{13}Fe_4$ phases are converted into small phases. The microstructure of the TIG + FSP region enhanced the variation of temperature in the stir zone, which improved the UTS. The effect of grain size on the precipitates, dislocation density, and solid solution was insignificant [54, 55]. Precipitate advancement comprises the dissolution, coarsening, and nucleation of the precipitate. In the FSP region, magnesium and silicon form strong precipitates of Mg_2Si, due to the precipitate of Mg_2Si. The TIG + FSP's hardness depends on the precipitate formation, strain hardening, and boundary energy.

The nucleation rate can be calculated as [56].

$$I = I0\exp\left[-\left(\frac{A_0}{RT}\right)^3\left(\frac{1}{\ln\overline{C}/C_e}\right)^2\right]\exp\left(-\frac{Q_d}{RT}\right) \quad (1)$$

The dissolution of precipitates may be written as

$$v = \frac{\overline{C} - C_i D}{C_p - C_i r} \quad (2)$$

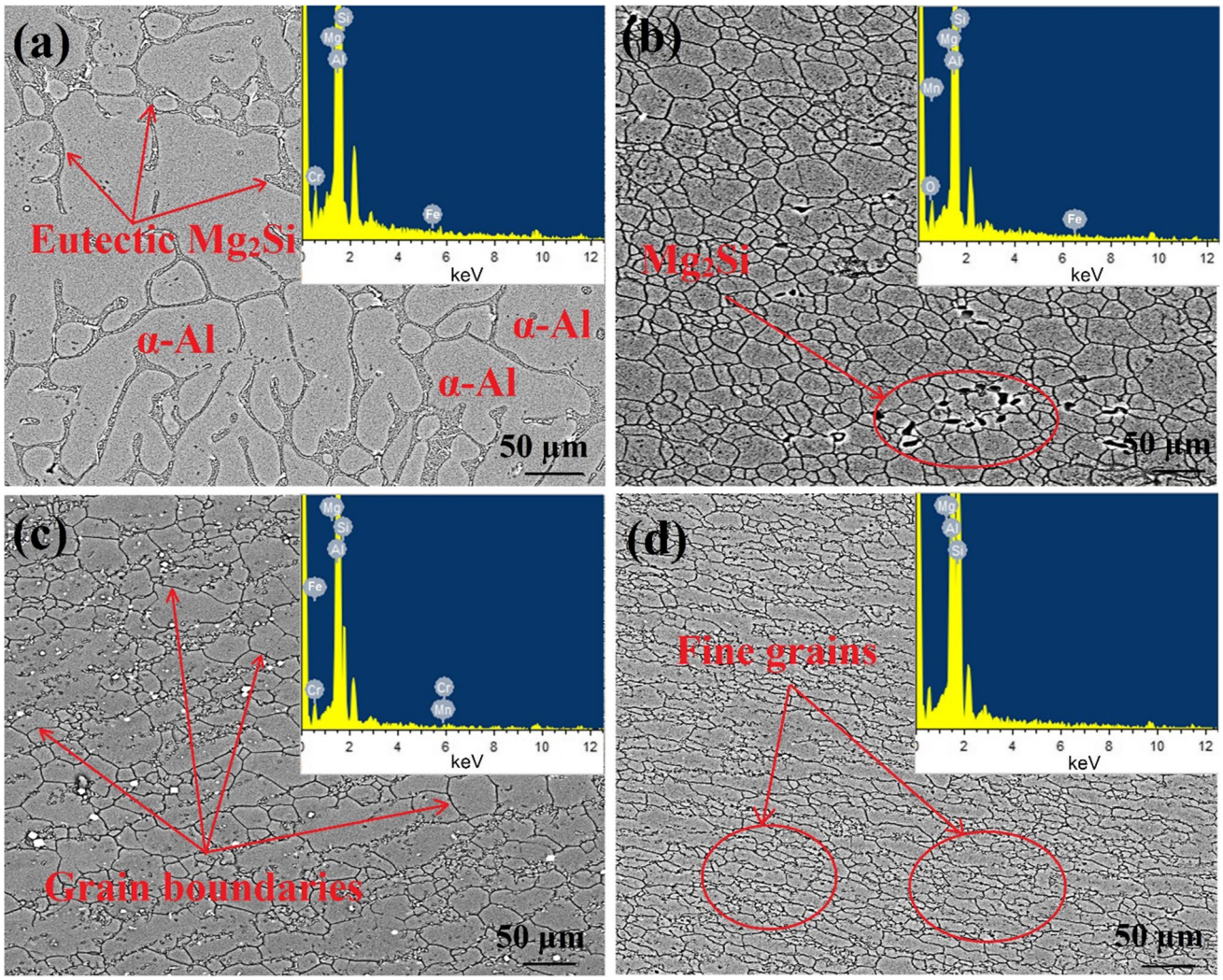

Fig. 7 SEM images of TIG and TIG + FSP welded joint, (**a**) TIG welded joint, (**b**) SZ of TIG + 1FSP, (**c**) SZ of TIG + 2FSP, (**d**) SZ of TIG + 3FSP

C_i can be calculated as following [57].

$$C_i = C_e \exp\left(\frac{2\gamma V_m}{rRT}\right) \tag{3}$$

The involvement to the yield strength (YS) from the hardening precipitates can be written as

$$\sigma_P = \frac{M}{b\bar{r}}\left(2\beta Gb^2\right)^{-1/2}\left(\frac{3f}{2\pi}\right)^{1/2}\left(\frac{\sum_i N_i F_i}{\sum_i N_i}\right)^{3/2} \tag{4}$$

$$F_i = 2\beta Gb^2\left(\frac{r_i}{r_c}\right) \tag{5}$$

When $r_i = r_c$ then $F_i = 2\beta Gb^2$
So, the YS can be evaluated as

$$\sigma_{ss} = k_{Fe}C_{Cu}{}^{2/3} + k_{Si}C_{Si}{}^{2/3} + k_{Mg}C_{Mg}{}^{2/3} \tag{6}$$

where.

R	8.314 J/K/mol.
Q_d	130kJ/mol.
A_0	Energy barrier for nucleation (16.22 kJ/mol).
r	Particle radius.
C_p	Concentration of element.
I_0	9.66×10^{34} s/m^3.
C_i	Concentration of solute.
Q_d	130 kJ/mol.
$\bar{r}$	Mean particle radius.
M	3.1 (Taylor factor).
b	2.84×10^{-10}.
Vm	3.95×10^{-5} m^3/mol.
k_{Mg}	Concentration of Mg.

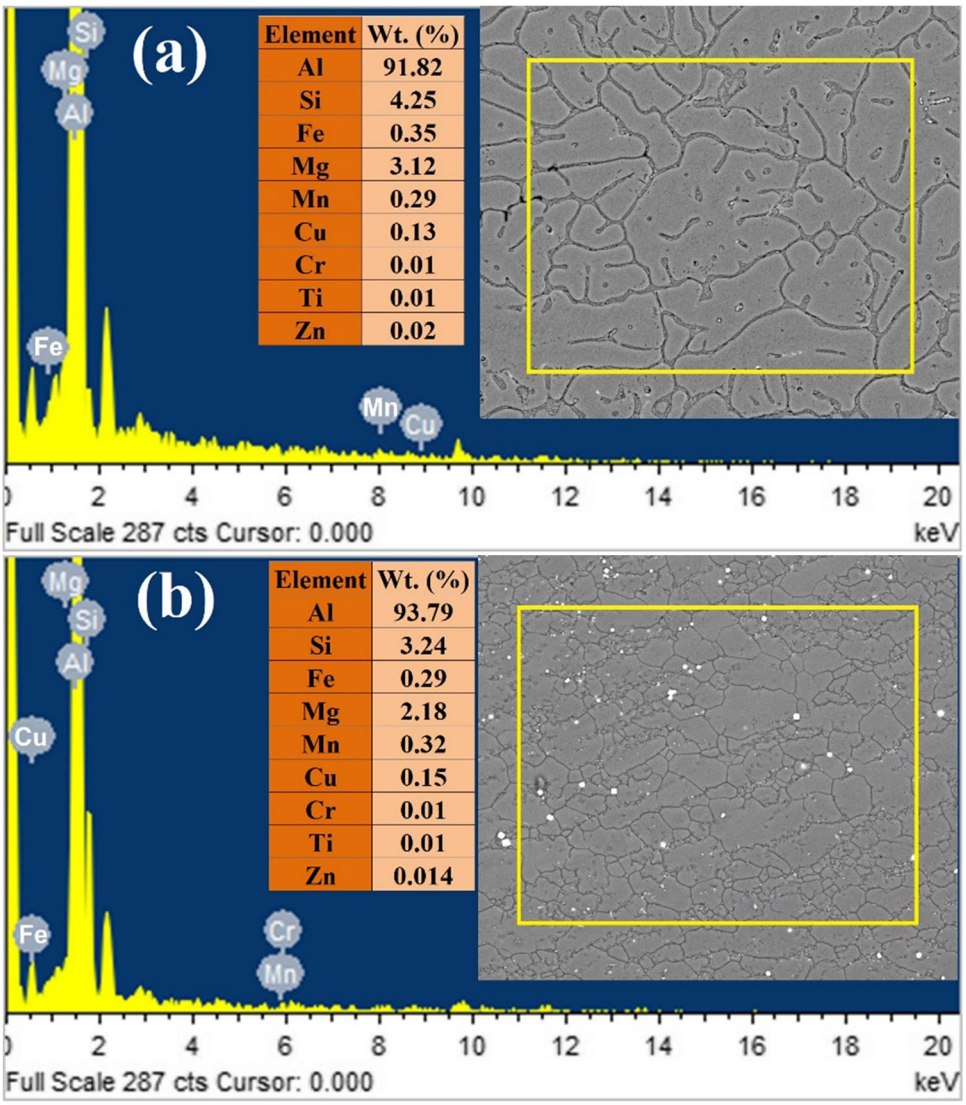

Fig. 8 EDS analysis, (**a**) TIG welded joint, (**b**) TIG + FSP welded joint

γ	Particle interface energy (0.2).
C_e	Equilibrium solute content in the matrix.
D	Diffusion coefficient.
C_{Cu}	Scaling factor of Cu.
F_i	Particle radius' function.
r_i	Particle radius.
$\bar{C}$	Mean solute content in the matrix.
N_i	Density number of the particles.
k_{Si}	Concentration of Si.
C_{Si}	Scaling factor of Si.
f	Volume fraction.
G	2.7×10^{-10} N/m^3.
β	Dissolution line tension (0.36).
C_{Mg}	Scaling factor of Mg.
k_{Cu}	Concentration of Cu.
r_c	Critical radius.

3.4 EBSD analysis of TIG and TIG + FSP welded joints

Figure 12 represents the EBSD diagram of the TIG and TIG+FSP weldments of AA5083 and A8011. The grain colors demonstrate the various grain orientations and crystallographic axes. The high angle grain boundaries (3-15°) and low angle grain boundaries (less than 15°) were marked in red and yellow color in the EBSD map. During FSP, the material flows in different fashions on the RS and the AS [58, 59]. The microstructure of the SZ was found systematically at the center and on the RS (3 mm from the center) and AS (3 mm from the center) sides. The transition from the AZ to the parent material through TMAZ and HAZ was also observed. The MPFSP refined the grain size of the TIG weldment. The amount of grain refinement is very significant, and the final grain size after FSP depends on the tool

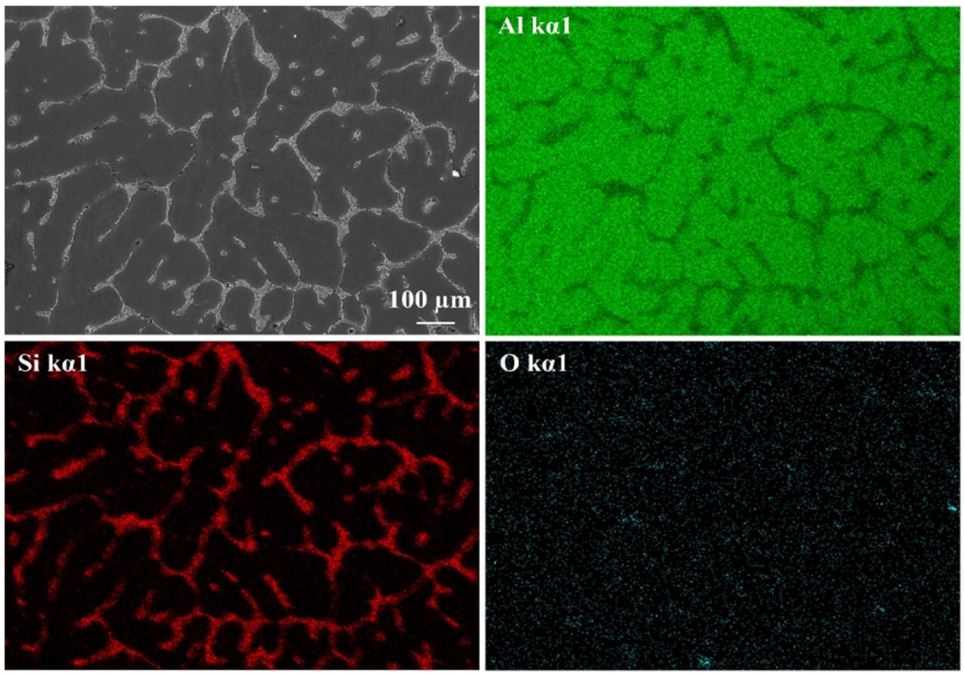

Fig. 9 Elemental mapping of TIG welded joint

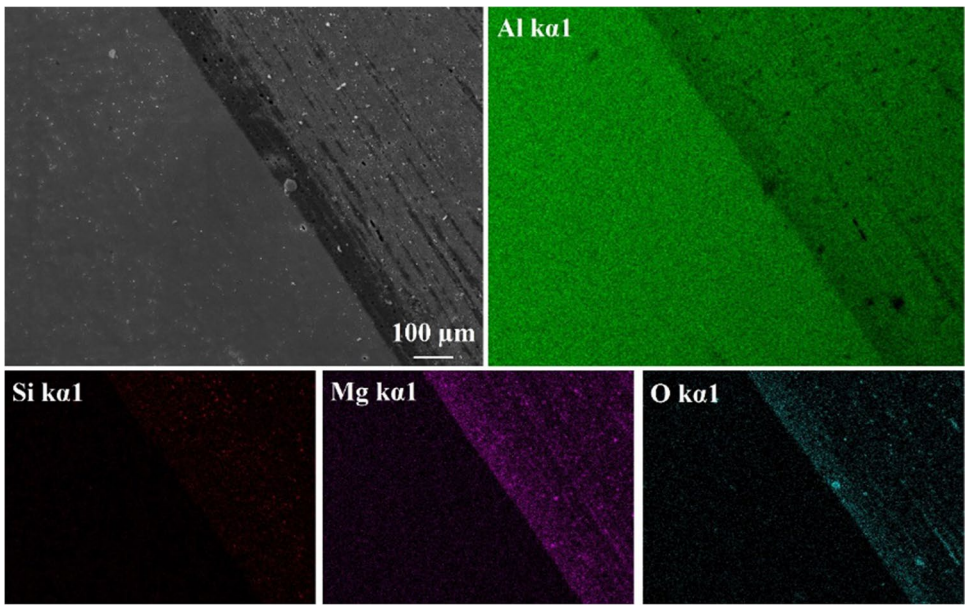

Fig. 10 Elemental mapping of TIG + FSP welded joint

geometry and processing parameters rather than the grain refinement occurring by the DRX. Apart from the coarse and inhomogeneous structure of the TIG welded joint, progressive DRX was observed as the FSP pass increased from one to three. The uniform color mixing in the TIG+FSP reveals the grain refinement, effective inter-metal mixing, and particle distribution. The microstructure modification and degree of grain reduction during TIG+FSP include acceleration flow, material preheating, deceleration flow, and high-velocity flow, which were attributed to continuous and discontinuous DRX, respectively [60, 61]. During deceleration, strain reversal induced grain modification was promoted. Figure 12b-d reveals the grain dissemination from the EBSD map of the TIG + FSP welded joint. As the FSP increased, the TIG+FSP composite's grain size was changed to be assisted by particle-induced pinning. The TIG+FSP welded joints observed higher DRX; this occurrence was attributed to the growth of the different nucleation sites and consequently decreasing the grain size within the SZ [62]. A frictional temperature of 0.55 to 0.75 times the melting point was observed for FSP composites for all the specimens. The temperature variation of each zone is shown

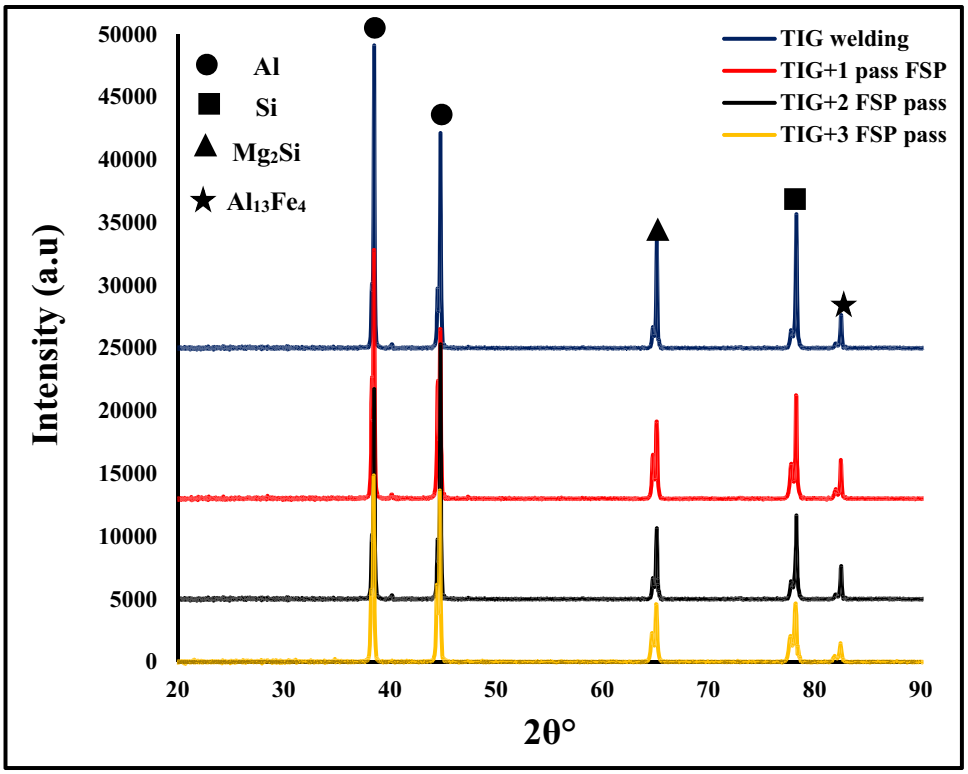

Fig. 11 XRD analysis of TIG and TIG + FSP welded joints of AA5083 and AA8011

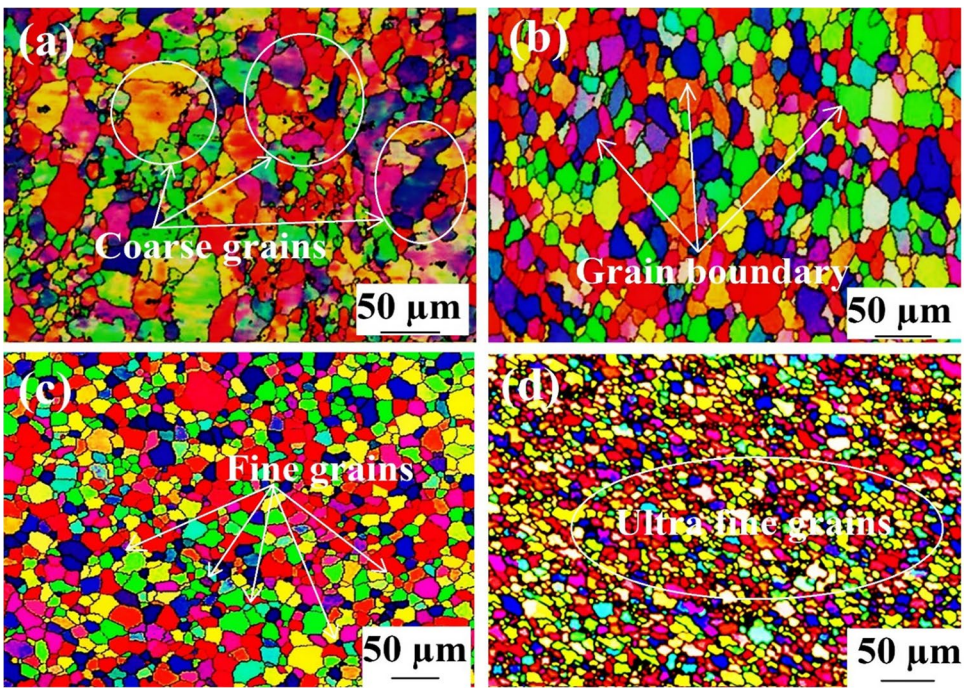

Fig. 12 EBSD image of welded joints of AA5083 and AA8011, (**a**) TIG welded joint, (**b**) TIG + 1pass FSP, (**c**) TIG + 2pass FSP, (**d**) TIG + 3pass FSP

in Table 5. Average grain size of 10.85 µm was observed in a single FSP pass that generates the fine and equiaxed grain structures illustrated in Fig. 12a. As the FSP passes increase, the grain modification occurs, and we observe an average grain size of 6.95 µm and 3.42 µm after 2 passes and 3 passes, respectively. The fine and equiaxed grain size of the composite MPFSP is correlated to DRX, followed by grain growth. The interaction between dislocations and reinforcement particles may lead to a higher density of stored dislocations [63, 64]. The fine grains contain a large

Table 5 Temperature ranges of TIG + FSP at different zones

Position	AA8011		SZ	AA5083	
	HAZ	TMAZ		TMAZ	HAZ
Temperature range (°C)	355–370	390–415	430–445	405–425	375–390

fraction of HAGBs, which reveals that a high fraction of LAGBs in the base metal was converted into HAGBs after FSP. The precipitation sequence in aluminum alloys was observed during MPFSP [27, 65]. The maximum grain size of the TIG + FSP weldment is about 1.5 to 2.5 times larger than the average grain size. The average grain size of the TIG+1 pass FSP, TIG+2 pass FSP, and TIG+3 pass FSP was around 10.85 µm, 6.95 µm, and 3.42 µm respectively. During TIG+FSP, severe plastic deformation and high temperatures will support the DRX [66]. Since HAGBs are more stable than LAGBs in AMCs, a high proportion of the HAGBs could contribute to the thermal stability of the TIG+FSP welded joints.

3.5 Tensile strength

The UTS of TIG and TIG + FSP welded joints of AA5083 and AA8011 was analyzed by universal testing machine. The fracture in the TIG weldments occurred in the HAZ because this region is the weakest among all zones. The TIG + 1 FSP pass specimen fractured at the TMAZ region, whereas the TIG + 2 FSP pass and TIG + 3 FSP pass specimens fractured at the base metal (AA8011), an indication of the increased UTS of the TIG + FSP joints due to the lack of a low hardiness region and the strengthened SZ. To investigate the exact UTS of the TIG + FSP weldment, the tensile specimens were cut along the FSP direction. The stress–strain diagram of the different processes reveals in Fig. 13.

The equiaxed and fine-grain structures with a large fraction of HAGBs obtained by TIG+FSP welded joints have a momentous influence on the UTS. The enhancement of the UTS of TIG+ FSP was primarily attributed to the significant grain modification. Furthermore, an enormous HAGBs fraction illustrates that enormous misorientation exists between the neighboring grains, which offers additional obstruction and increases the resistance against grain boundaries interrupted by dislocation, resulting in grain boundary strengthening [67, 68]. Moreover, the 2nd phase crystals with homogenous dissemination act as dominant barriers to dislocation motion, increasing the TIG+FSP region's UTS [69]. The grain refinement helps to enhance the compatibility of neighboring grains and thus improves the percentage strain. The uniform dissemination of the fine 2nd phase crystals was responsible for the enhancement of the percentage strain. The base metal (AA5083 and AA8011) exhibits a UTS of 320.89 MPa and 93.07 MPa, while the % strain is 27.9 and 39.1 respectively. Due to welding defects and coarse grain structure in the FZ, the TIG welded joints reveal a minimum UTS of 79.82 MPa. After FSP on TIG weldment, the UTS and % strain increased. A maximum UTS of 126.92 MPa was observed in TIG+3pass FSP illustrated in Table 4. Due to the significant grain refinement and

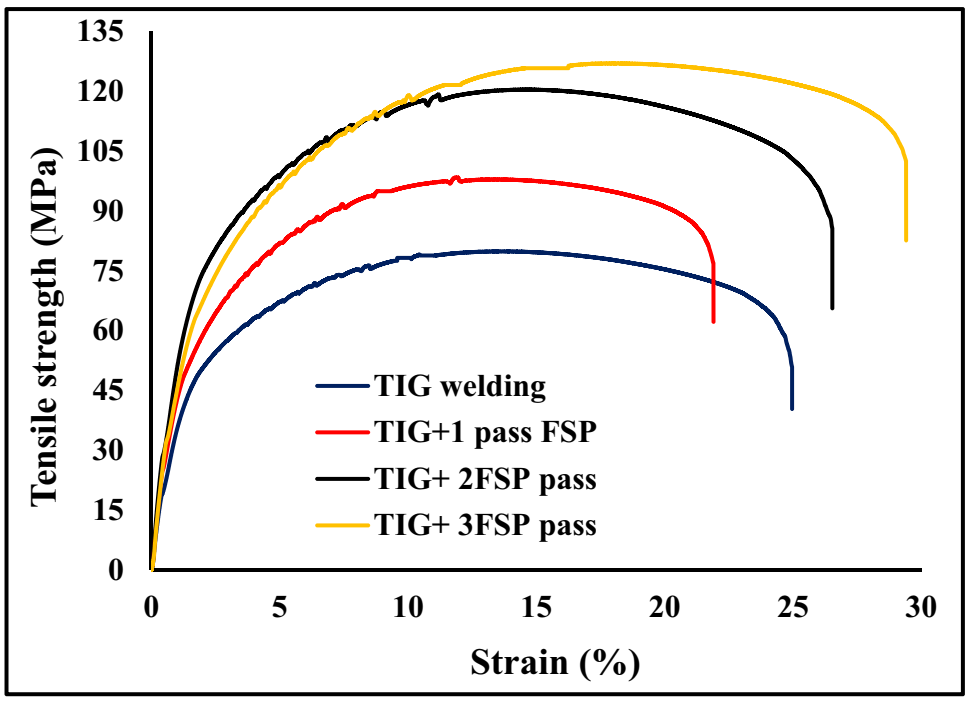

Fig. 13 Stress strain diagram of TIG and TIG + FSP welded joint of AA5083 and AA8011

dissolution of coarse Mg_2Si, and $Al_{13}Fe_4$ phases. Moreover, the dissolution of coarse Mg_2Si and $Al_{13}Fe_4$ phases can significantly decrease the crack's growth rate and enhance the ductility of TIG+FSP welded joints.

3.6 Microhardness of TIG and TIG + FSP welded joints

The hardness distribution profile of TIG and TIG+FSP weldments of AA5083 and AA8011 is illustrated in Fig. 14. The microhardness variation may be related to the microstructure of the welded region. The variations in the hardness values show the non-uniformity of grain structures. The grain structure or grain size may be the dominating factor in determining the hardness value, but it is not the only one. Temperature distribution, strain rate, and particle density seem to affect the hardness of the welded region [70]. The decrease in temperature causes an increase in strain hardening. As a result, smaller grain size, as well as strain rate at low temperature-induced strain hardening of the TIG+FSP, welded joints. In TIG welded joints, the HAZ region exhibits the lowest hardness due to the combined mixture of ER4043 and base metal in the TIG welded region. The hardness distribution pattern for TIG + FSP welded joints was similar to that of TIG-welded joints but different from that of TIG-welded joints. The inhomogeneity of microhardness in the SZ is due to inadequate material flow engendered by the FSP tool [71]. As per the Hall-Petch correlation, the fine grain structure was observed to have a higher hardness at room temperature. A large fluctuation was seen in the TIG weldments compared to the TIG + FSP welded joints. This is due to the TIG joints' being composed of coarse Mg_2Si and $Al_{13}Fe_4$ precipitating intermetallic phases. The α-Al phase weaker than the Mg_2Si, and $Al_{13}Fe_4$ phases, has an enormous volume fraction. The hardness value would be lower if the indenter was placed near the primary α-Al phase rather than the Mg_2Si phase in the opposite condition, the hardness value was observed to be high.

The hardness value of the TIG weldment was lower than the TIG+FSP weldments. The average hardness value of TIG weldment at the FZ was observed to be 52 HV, whereas the hardness value at the SZ of TIG + FSP welded joints of 1 pass, 2 passes, and 3 passes were found to be 60.3 HV, 64.8 HV, and 68 HV, respectively. Along with grain coarsening, the strengthening phase coarsens and partially dissolves in the HAZ, resulting in a steady fall in hardness in the HAZ. Most precipitates were found to dissolve in the TMAZ region [72]. With the Sharpe grain size gradient and high-stress concentration, the occurrence of the worst tensile properties was observed in the TMAZ region. The fracture at the TMAZ region can have occurred due to the heat effect, non-uniform microstructure, and distortion. It was also found that the dissolution and defects of the precipitate were created by inadequate heat input, which had a deleterious effect on the performance of welded joints [73]. So, the TIG+FSP welded joint with the finest tensile properties was observed with adequate heat input with the 3rd FSP pass.

3.7 Fractography

The fracture surface of the TIG and TIG + FSP welded joints (Fig. 15) of AA5083 and AA8011 was analyzed under SEM. In tensile specimens, the shear plane of 45° (approximately) to the tensile axis is observed along the peripheral of the test specimens [74, 75]. The cup cone fracture was observed in the TIG + FSP welded joints. The fracture surface of TIG and TIG + FSP welded joints characterized by the cleavage facets, tear ridges, deep dimples

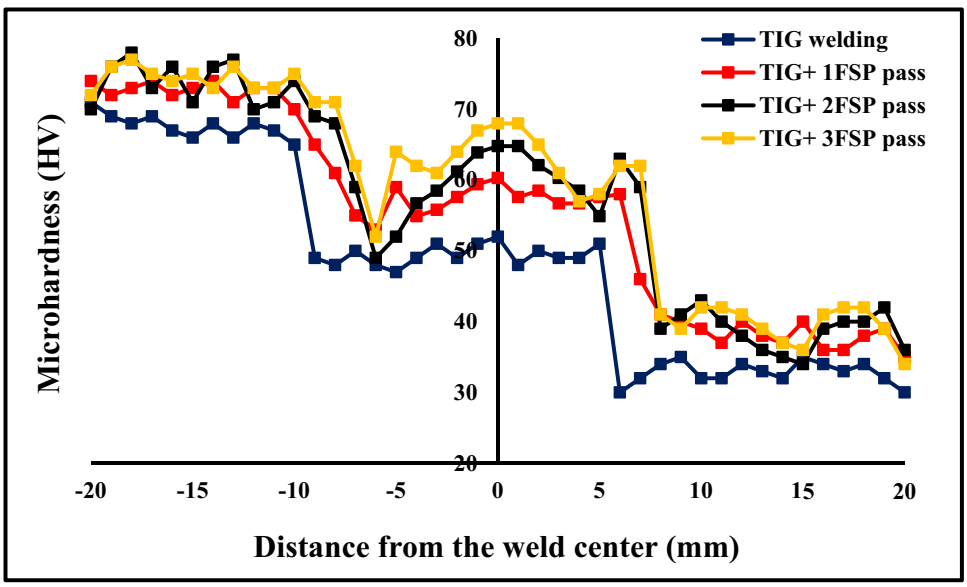

Fig. 14 Hardness distribution profile of TIG and TIG + FSP welded joints of AA5083 and AA8011

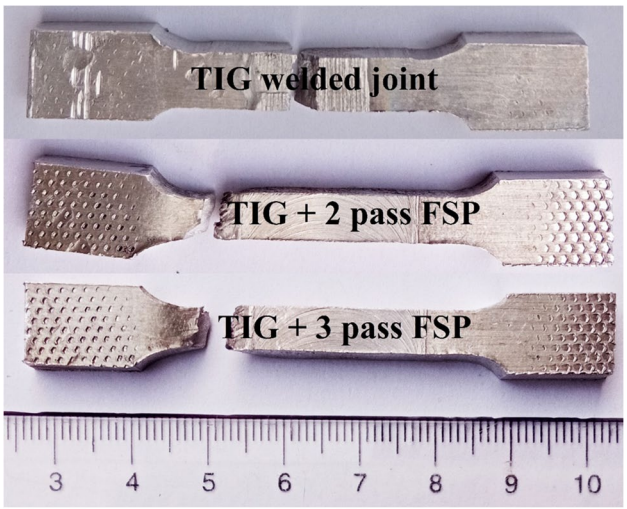

Fig. 15 Fractured specimens of TIG and TIG + FSP

and ductile dimples as shown in Fig. 16. TIG welded joint consisted deep dimples resulting from the microvoids coalescence with cleavage facets. The large area of fine and ductile dimples was observed in the TIG + 3 pass FSP, whereas ductile dimples with tear ridge, and cleavage facets was observed in the TIG + 1 pass FSP and 2 pass FSP. In TIG + 1 pass FSP, the particles were redistributed and refined. Because the redistribution removes the dendritic structure to a greater extent, inter-dendritic crack propagation was prevented and the cracks were disseminated through the aluminum base. The heat input and the TRS were observed to have a linear correlation, which affects the joint's efficiency. When the TRS increases, heat input also increases, which influences the grain size of SZ. However, as the heat input increased, the grain size of the HAZ also increased, resulting in a reduction in tensile properties. This phenomenon encouraged the fracture to occur in the HAZ region in TIG + 1 pass FSP [76, 77]. Meanwhile, the aluminum base zone was ductile. The dissemination of cracks through the aluminum base led to improved ductility. This leads to the formation of micro dimples in the ruptured surface was observed in the TIG + FSP welded joints shown in Fig. 16. The ruptured interface with cleavage and dimples was the foremost reason for the fraction. Figure 16 reveals a network of fine dimples in TIG + 2 pass FSP and TIG + 3 pass FSP, indicating a ductile failure. Conversely, a distinct difference in the size of the dimples may be observed between the TIG and TIG + FSP welded joints. Large voids and dimples were easily visible in the TIG welded joint shown in Fig. 16a, whereas fine and more uniform-sized dimples in the TIG + 3 pass FSP were observed as compared to the TIG welded joint.

4 Conclusions

The tensile properties and microstructural evaluation of TIG and TIG + FSP of dissimilar aluminum alloys of AA8011 and AA5083 were successfully carried out and the following conclusions were made.

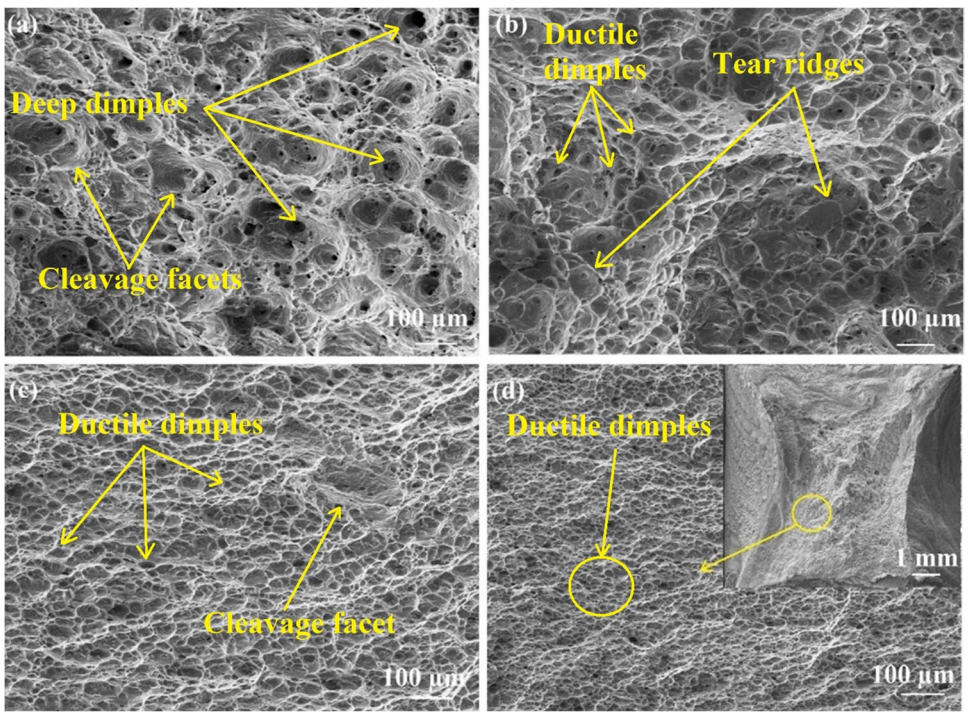

Fig. 16 Fractography images of welded joint of AA5083 and AA8011, (**a**) TIG welded joint, (**b**) TIG + 1pass FSP, (**c**) TIG + 2pass FSP, (**d**) TIG + 3pass FSP

- The multipass FSP was employed on Si-rich TIG welded joint of AA5083 and AA8011. The TIG welding defects were eliminated, and the grain size of the TIG welded joint was decreased. As the FSP passes increases, the coarse eutectic Mg_2Si and $Al_{13}Fe_4$ phases are converted into small phases.
- The homogenization or modification of the primary α-Al exists in the TIG weldment was continuously improved as the TIG + FSP pass increased. The coarse and elongated dendrite structure of the TIG welded joint was decreased as the FSP passes increased.
- Due to the enhancement of material mixing and dispersion, the eutectic Mg_2Si precipitates were further decimated. The TIG + FSP welded joints observed higher DRX; this occurrence was attributed to the growth of the different nucleation sites and consequently decreasing the grain size within the SZ.
- The fine and equiaxed grain size of the composite MPFSP is correlated to DRX, followed by grain growth. The interaction between dislocations and reinforcement particles may lead to a higher density of stored dislocations. The fine grains contain a large fraction of HAGBs, which reveals that a high fraction of LAGBs in the base metal was converted into HAGBs after FSP.
- The average UTS of the TIG welded joint with filler ER4043 was observed to be 79.82 MPa, whereas the UTS of TIG + 1 pass FSP, TIG + 2 pass FSP, and TIG + 3 pass FSP was 97.87 MPa, 120.36 MPa, and 126.92 MPa respectively. The average grain size of the TIG + 1 pass FSP, TIG + 2 pass FSP, and TIG + 3 pass FSP was around 10.85 µm, 6.95 µm, and 3.42 µm respectively.
- During TIG + FSP, severe plastic deformation and high temperatures will support the DRX. Since HAGBs are more stable than LAGBs in AMCs, a high proportion of the HAGBs could contribute to the thermal stability of the TIG + FSP welded joints.

Acknowledgements The authors would like to express heartfelt thanks to Department of Mechanical engineering, Cape Peninsula University of Technology, South Africa for providing the experimental setup and their corresponding labs for supporting this work.

Author contributions Abdellah Nait Salah: Data curation, Writing-original draft preparation.

Sipokazi Mabuwa, and Velaphi Msomi: Conceived and planned the experiments, and carried out the experiments.

Husain Mehdi: Paper writing, and reviewing.

Mohammed Kaddami: Reviewing and editing.

Prabhujit Mohapatra: Editing and Visualization.

Data Availability Not applicable.

Declarations

Conflict of Interest Authors declare no conflict of interest.

Compliance with ethical standards The authors have declared that no competing interests exist.

Consent to participate Not applicable.

Consent for Publication Not applicable.

References

1. Mishra RS, Ma ZY, Charit I (2003) Friction stir processing: a novel technique for fabrication of surface composite. Mater. Sci. Eng. A 341(1–2):307–310
2. Husain M, Mishra RS (2021) Effect of multi-pass friction stir processing and SiC nanoparticles on microstructure and mechanical properties of AA6082-T6. Adv Ind Manuf Eng 3:100062. https://doi.org/10.1016/j.aime.2021.100062
3. Husain Mehdi, R.S. Mishra, Study of the influence of friction stir processing on tungsten inert gas welding of different aluminum alloy. SN Appl. Sci. 1, 712 (2019). https://doi.org/10.1007/s42452-019-0712-00.
4. Fayomi J, Popoola API, Popoola OM, Fayomi OSI, Ajenifuja E (2021) Response evaluation of AA8011 with nano ZrB2 inclusion for multifunctional applications: Considering its thermal, electrical, and corrosion properties. Journal of Alloys and Compounds 853:157197
5. Huang Chuanjun, Zhixiong Wu, Huang Rongjin, Wang Wei, Li Laifeng (2017) Mechanical properties of AA5083 in different tempers at low temperatures. IOP Conf. Series: Materials Science and Engineering 279:012002
6. Saini N, Pandey C (2018) Dheerendra Kumar Dwivedi, Ductilizing of cast hypereutectic Al–17%Si alloy by friction stir processing. Proceedings of the Institution of Mechanical Engineers, Part E: Journal of Process Mechanical Engineering 232(6):696–701
7. Saini N, Pandey C, Thapliyal S et al (2018) Mechanical Properties and Wear Behavior of Zn and MoS2 Reinforced Surface Composite Al- Si Alloys Using Friction Stir Processing. SILICON 10:1979–1990
8. Deepan M, Pandey C, Saini N et al (2017) Estimation of strength and wear properties of Mg/SiC nanocomposite fabricated through FSP route. J Braz Soc Mech Sci Eng 39:4613–4622
9. Fayomi J, Popoola API, Popoola OM, Oladijo OP, Fayomi OSI (2019) Tribological and microstructural investigation of hybrid AA8011/ZrB2-Si3N4 nanomaterials for service life improvement. Results Phys. 14:102469
10. Li Quan Wu, Ai-ping Zhao Yue, Guo-qing Wang, Dong-yang Yan, Hui-qiang Wu (2015) Fracture behavior of double-pass TIG welded 2219–T8 aluminum alloy joints under transverse tensile test [J]. Transactions of Nonferrous Metals Society of China 25(6):1794–1803
11. Takhti S, Reihanian M, Ashrafi A (2015) Microstructure characterization and mechanical properties of gas tungsten arc welded cast A356 alloy. Trans Nonferrous Met Soc China 25(7):2137–2146. https://doi.org/10.1016/S1003-6326(15)63825-0
12. Chen YB, Lei ZL, Li LQ, Wu L (2006) Experimental study on welding characteristics of CO2 laser TIG hybrid welding process. Sci Technol Weld Joining 11(4):403–411
13. Song G, Luo Z (2011) the influence of laser pulse waveform on laser–TIG hybrid welding of AZ31B magnesium alloy. Opt Lasers Eng 49(1):82–88

14. A. El-Batahgy and M. Kutsuna, "Laser beam welding of AA5052, AA5083, and AA6061 aluminum alloys, Advances in Materials Science and Engineering, 2009, 1–9. https://doi.org/10.1155/2009/974182.
15. Verma Rajesh P, Pandey KN, Sharma Yogesh (2015) Effect of ER4043 and ER5356 filler wire on mechanical properties and microstructure of dissimilar aluminium alloys, 5083-O and 6061–T6 joint, welded by the metal inert gas welding. Proceedings of the Institution of Mechanical Engineers, Part B: Journal of Engineering Manufacture 229(6):1021–1028
16. Elanchezhian C, VijayaRamnath B, Venkatesan P, Sathish S, Vignesh T, Siddharth RV, Vinay B, Gopinath K (2014) Parameter Optimization of Friction Stir Welding of AA8011–6062. Procedia Engineering 97:775–782
17. Mehdi Husain, Mishra RS (2021) Microstructure and mechanical characterization of TIG-welded joint of AA6061 and AA7075 by friction stir processing. Proceedings of the Institution of Mechanical Engineers, Part L: Journal of Materials: Design and Applications 235(11):2531–2546
18. Mehdi Husain, Mishra RS (2020) Influence of friction stir processing on weld temperature distribution and mechanical properties of TIG welded joint of AA6061 and AA7075. Transactions of the Indian Institute of Metals 73:1773–1788
19. Mehdi Husain, Mishra RS (2020) Effect of Friction Stir Processing on Microstructure and Mechanical Properties of TIG Welded Joint of AA6061 and AA7075. Metallography, Microstructure, and Analysis 9:403–418
20. Mehdi Husain, Mishra RS (2020) Investigation of mechanical properties and heat transfer of welded joint of AA6061 and AA7075 using TIG+FSP welding approach. Journal of Advanced Joining Processes 1:100003
21. Takhti S, Reihanian M, Ashrafi A (2015) Microstructure characterization and mechanical properties of gas tungsten arc welded cast A356 alloy. Trans Nonferrous Met Soc China 25:2137–2146
22. Chen Y-B, Miao Y-G, Li L-Q, Lin Wu (2009) Joint performance of laser-TIG double-side welded 5A06 aluminum alloy. Transactions of Nonferrous Metals Society of China 19(1):26–31
23. Chen Y-B, Miao Y-G, Li L-Q, Lin Wu (2008) Arc characteristics of laser-TIG double-side welding. Sci Technol Weld Joining 13(5):438–444
24. Shen J, Xu N (2012) Effect of preheat on TIG welding of AZ61 magnesium alloy. Int J Miner Metall Mater 19:360–363
25. Ramana Venkat, Yelamasetti Balram, Vardhan Vishnu (2021) Study on weldability and effect of post heat treatment on mechanical and metallurgical properties of dissimilar AA 2025, AA 5083 and AA7075 GTAW weld joints. Materials today proceedings 46(1):878–882
26. Husain Mehdi RS (2021) Mishra, Effect of Friction Stir Processing on Mechanical Properties and Wear Resistance of Tungsten Inert Gas Welded Joint of Dissimilar Aluminum Alloys. Journal of Material Engineering and Performance 30:1926–1937
27. Su JQ, Nelson TW, Mishra R, Mahoney M (2003) Microstructural investigation of friction stir welded 7050–T651 aluminium. Acta Mater 51:713–729
28. Thomas WM, Nicholas ED, Needham JC, Murch MG, Temple-Smith P, Dawes CJ (1991) Friction stir butt welding. International Patent Application No. PCT/GB92/02203; 1991. G.B. Patent Application No. 9125978.8
29. Mishra RS, Ma ZY (2005) Friction stir welding and processing. Mater Sci Eng R Rep 50:1–78
30. A Nait Salah, Husain Mehdi, Arshad Mehmood, Abdul Wahab Hashmi, Chandrabhanu Malla, Ravi Kumar, Optimization of process parameters of friction stir welded joints of dissimilar aluminum alloys AA3003 and AA6061 by RSM, materials today proceedings, 2021, https://doi.org/10.1016/j.matpr.2021.10.288.
31. Sadoun AM, Wagih A, Fathy A, Essa ARS (2019) Effect of tool pin side area ratio on temperature distribution in friction stir welding. Results in Physics 15:102814
32. Mastanaiah P (2016) Abhay Sharma G, Madhusudhan Reddy, Dissimilar Friction Stir Welds in AA2219-AA5083 AluminiumAlloys: Effect of Process Parameters on Material Inter-Mixing. Defect Formation, and Mechanical Properties, Trans Indian Inst Met 69(7):1397–1415
33. Taban E, Kaluc E (2006) Microstructural and mechanical properties of double-sided MIG, TIG and friction stir welded 5083–H321 aluminium alloy. Kovove Mater 44:25–33
34. Mabuwa S, Msomi V (2020) The impact of submerged friction stir processing on the friction stir welded dissimilar joints. Mater. Res. Express 7:096513
35. Singh D, Rao PN, Jayaganthan R (2013) Effect of Deformation Temperature on Mechanical Properties of Ultrafine Grained Al – Mg Alloys Processed by Rolling. Mater Des 50:646–655
36. Lee YB, Shin DH, Park KT, Nam WJ (2004) Effect of Annealing Temperature on Microstructures and Mechanical Properties of a 5083 Al Alloy Deformed at Cryogenic Temperature. Scr Mater 51(4):355–359
37. Ma ZY (2008) Friction stir processing technology: a review. Metall Mater Trans A 39:642–658. https://doi.org/10.1007/s11661-007-9459-0
38. Su JQ, Nelson TW, Sterling CJ (2006) Grain Refinement of Aluminum Alloys by Friction Stir Processing. Philos Mag 86(1):1–24
39. Rastkerdar E, Shamanian M, Saatchi A (2013) Taguchi optimization of pulsed currentGTA welding parameters for improved corrosion resistance of 5083 aluminumwelds. J Mater Eng Perform 22(4):1149–1160
40. Liu Y et al (2012) Microstructure and mechanical properties of aluminum 5083weldments by gas tungsten arc and gas metal arc welding. Mater Sci Eng A 549:7–13
41. Guo Y et al (2018) An investigation on plasma-MIG hybrid welding of 5083 aluminum alloy. Int J Adv Manuf Technol 98(5–8):14331440
42. Wang J, Zhou D, Xie L, Li X, Lu Y, Bai Z, Zhou J (2021) Effect of multi-pass friction stir processing on microstructures and mechanical behaviors of as-cast 2A14 aluminum alloy. J Mater Eng Perform 30:3033–3043
43. Chen Y, Ding H, Cai Z, Zhao J, Li J (2016) Effect of initial base metal temper on microstructure and mechanical properties of friction stir processed Al-7B04 alloy Mater. Sci Eng A 650:396–403
44. Wang J, Yang K, Zhou D, Xie L, Lu Y, Li X (2021) Investigation on the microstructures and mechanical properties of friction stir processed 2A14 aluminum alloy fabricated by different initial precipitation states, The Int. J. Adv. Manuf. Technol. 116:3549–60
45. He XC, Gu FS, Ball A (2014) A review of numerical analysis of friction stir welding. Prog Mater Sci 65:1–66
46. Liu LM, Song G, Liang GL, Wang JF (2005) Mater Sci Eng A 390:76–80
47. Duan S, Matsuda K, Zou Y, Wang T (2019) Influence of two-stage ageing process and Cu additions on conductive Al alloys based on AA 6063. Materials Research Express 6:106509
48. Barmouz M, BesharatiGivi MK, Seyfi J (2011) On the role of processing parameters in producing Cu/SiC metal matrix composites via friction stir processing: investigating microstructure, microhardness, wear and tensile behavior. Mater. Charact. 62:108–117
49. Barmouz M, BesharatiGivi MK (2011) Fabrication of in situ Cu/SiC composites using multi-pass friction stir processing: evaluation of microstructural, porosity, mechanical and electrical behavior. Compos. Part A 42(10):1445–1453
50. Su P, Gerlich A, North TH, Bendzsak GJ (2013) Material flow during friction stir spot welding. Sci Technol Weld Joining 11(1):61–71
51. Zhang Z, Chen DL (2006) Consideration of Orowan strengthening effect in particulate-reinforced metal matrix nanocomposites: A model for predicting their yield strength Author links open overlay panel. Scripta Materialia 54(7):1321–1326

52. Chang CI, Lee CJ, Huang JC (2004) Relationship between grain size and Zener-Holloman parameter during friction stir processing in AZ31 Mg alloys. Scripta Mater 51:509–514
53. Oladijo OP, Venter AM, Cornish LA, Sacks N (2012) X-ray diffraction measurement of residual stress in WC-Co thermally sprayed coatings onto metal substrates. Surf Coat Techno 206:4725–4729
54. Paidar M (2019) Olatunji Oladimeji Ojo, Hamid Reza Ezatpour, Influence of multi-pass FSP on the microstructure, mechanical properties and tribological characterization of Al/B C composite fabricated by accumulative roll bonding (ARB). Surf Coat Technol 361:159–169
55. Pandey Chandan, AnojGiri MM (2016) Mahapatra, Evolution of phases in P91 steel in various heat treatment conditions and their effect on microstructure stability and mechanical properties. Materials Science & Engineering A 664:58–74
56. Simar A, Brechet Y, Meester BD, Denquin A, Gallais C, Pardoen T (2012) Integrated Modeling of Friction Stir Welding of 6xxx Series Al Alloys: Process Microstructure and Properties. Prog Mater Sci 57:95–183
57. Zhang Z, Wan ZY, Lindgren LE, Tan ZJ, Zhou X (2017) The Simulation of Precipitation Evolutions and Mechanical Properties in Friction Stir Welding with Post Weld Heat Treatments. J Mater Eng Perform 26:5731–5740
58. McNelley TR, Swaminathan S, Su JQ (2008) Recrystallization mechanisms during friction stir welding/processing of aluminum alloys. Scripta Mater 58:349–354
59. Seidel TU, Reynolds AP (2001) Visualization of the material flow in AA2195 friction-stir welds using a marker insert technique. Metall Mater Trans A 32:2879–2884
60. Srivastava M, Rathee S, Siddiquee AN (2019) Investigation on the Effects of Silicon Carbide and Cooling Medium during Multi-Pass FSP of Al-Mg/ SiC Surface Composites. SILICON 11:2149–2157
61. Mehdi H, Mishra RS (2021) Consequence of reinforced SiC particles on microstructural and mechanical properties of AA6061 surface composites by multi-pass FSP. J Adhes Sci Technol. https://doi.org/10.1080/01694243.2021.1964846
62. Moradi MM, Aval HJ, Jamaati R, Amirkhanlou S, Ji S (2018) Microstructure and texture evolution of friction stir welded dissimilar aluminum alloys: AA2024 and AA6061. J Manuf Process 32:1–10
63. Liu XC, Sun YF, Nagira T, Ushioda K, Fujii H (2019) Evaluation of dynamic development of grain structure during friction stir welding of pure copper using a quasi in situ method. J Mater Sci Technol 35:1412–1421
64. Barmouz M, BesharatiGivi MK (2011) Fabrication of in situ Cu/SiC composites using multi-pass friction stir processing: evaluation of microstructural, porosity, mechanical and electrical behavior. Compos. Part A Appl. Sci. Manuf. 42:1445–1453
65. Lang P, Povoden-Karadeniz E, Falahati A, Kozeschnik E (2014) Simulation of the effect of composition on the precipitation in 6xxx Al alloys during continuous-heating DSC. J. Alloys Compd. 612:443–449
66. Liu FC, Ma ZY (2010) Contribution of grain boundary sliding in low-temperature superplasticity of ultrafine-grained aluminum alloys. Scr Mater 62:125–128
67. Paidar M, Asgari A, Ojo OO, Saberi A (2018) Mechanical properties and wear behavior of AA5182/WC nanocomposite fabricated by friction stir welding at different tool traverse speeds. J Mater Eng Perfor 27:1714–1724
68. Sharma DK, Patel V, Badheka V, Mehta K, Upadhyay G (2019) Fabrication of hybrid surface composites AA6061/(B4 C+MoS) via friction stir processing. J Tribolo 141(5):52201–52210
69. Husain Mehdi, R.S. Mishra, An experimental analysis and optimization of process parameters of AA6061 and AA7075 welded joint by TIG+FSP welding using RSM, Advances in Materials and Processing Technologies, 2020, https://doi.org/10.1080/2374068X.2020.1829952.
70. Tariq M, Khan I, Hussain G, Farooq U (2019) Microstructure and micro-hardness analysis of friction stir welded bi-layered laminated aluminum sheets. International Journal of Lightweight Materials and Manufacture 2(2):123–130
71. Patel VV, BadhekaVand Kumar A (2017) Effect of polygonal pin profiles on friction stir processed superplasticity of AA7075 alloy. J. Mater. Process. Technol. 240:68–76
72. Qin H, Zhang Hand WuH (2015) The evolution of precipitation and microstructure in friction stir welded 2195–T8 Al–Li alloy Mater. Sci. Eng. A 626:322–329
73. Chaurasia PK, Pandey C, Giri A, Saini N, Mahapatra MM (2018) a comparative study of residual stress and mechanical properties for fsw and tig weld on structural steel. Arch Metall Mater 63:1019–1029
74. Pandey C, Saini N (2017) Manas Mohan Mahapatra, Pradeep Kumar, Study of the fracture surface morphology of impact and tensile tested cast and forged (C&F) Grade 91 steel at room temperature for different heat treatment regimes. Eng Fail Anal 71:131–147
75. ChandanPandey MM, Mahapatra Pradeep Kumar, Prakash Kumar N, Saini J.G. Thakare (2019) Study on effect of double austenitization treatment on fracture morphology tensile tested nuclear grade P92 steel. Engineering Failure Analysis 96:158–167
76. Msomi Velaphi, Mabuwa Sipokazi (2020) Analysis of material positioning towards microstructure of the friction stir processed AA1050/AA6082 dissimilar joint. Advances in Industrial and Manufacturing Engineering 1:100002
77. Orłowska Marta, Brynk Tomasz, Hütter Andreas, Enzinger Norbert, Olejnik Lech, Lewandowska Małgorzata (2020) Similar and dissimilar welds of ultrafine grained aluminium obtained by friction stir welding. Materials Science and Engineering: A 777:139076